

# Characterizing the Influence of Charge Extraction Layers on the Performance of Triple-Cation Perovskite Solar Cells

Johanna Siekmann, Ashish Kulkarni,\* Samah Akel, Benjamin Klingebiel, Michael Saliba, Uwe Rau, and Thomas Kirchartz\*

Selecting suitable charge transport layers and suppressing non-radiative recombination at interfaces with the absorber layer is vital for maximizing the efficiency of halide perovskite solar cells. In this study, high-quality perovskite thin films and devices are fabricated with different fullerene-based electron transport layers and different self-assembled monolayers as hole transport layers. Then, a comparative study of a significant variety of different electrical, optical, and photoemission-based characterization techniques is performed to quantify the properties of the solar cells, individual layers, and, importantly, the interfaces between them. In addition, the limitations and problems of the different measurements, the insights gained by combining different methods, and the different strategies for extracting information from the experimental raw data, are highlighted.

## 1. Introduction

Electron and hole transport layers for lead-halide perovskite solar cells must fulfill several requirements simultaneously:<sup>[1]</sup>

a) provide low recombination at their interfaces to the absorber layer (passivation),<sup>[2–4]</sup> b) provide the appropriate band energy alignments to the absorber layer to allow efficient extraction of one type of charge carrier while blocking the other one<sup>[5,6]</sup> (selectivity), and c) minimize optical losses (parasitic light absorption) and resistive losses. In particular, in inverted or p-i-n structured perovskite solar cells, choosing the best charge transport layers (CTLs) is challenging because there is a multitude of different candidates to choose from, including a variety of self-assembled monolayers (SAM),<sup>[7,8]</sup> polymers, or fullerene derivatives.<sup>[9]</sup> To avoid having to

choose randomly and to perform a trial-and-error-based optimization, gaining insights into the effect of charge-transport layers on the performance, recombination, and charge collection in perovskite solar cells is of critical importance.<sup>[10–12]</sup> There is a large amount of literature dealing with perovskite–CTL interfaces showing that the modification of perovskite surfaces<sup>[5,6,13,14]</sup>, as well as the choice of suitable transport layers, frequently has a considerable influence on device performance.<sup>[2,7,8,15,16]</sup> However, characterization of the interfaces and interlayers is often performed using a set of individual methods, whose results are presented separately and often without any quantitative or model-based analysis. What is typically missing are experimentally determined parameters of the interface or the CTL that are quantitatively consistent with solar cell performance. Furthermore, there is typically a lack of comparisons between different measurement methods as well as consistency checks that critically examine the experimentally obtained parameters. The consequence of this situation is that trends are reported, while the community is still quite far from being able to perform quantitative characterization that could be validated with a model of the interfaces and the device.


Here, we apply a set of state-of-the-art characterization methods to triple-cation perovskite samples, employing a range of different electron and hole transport layers. The methods used include electrical characterization, optical spectroscopy, and surface physical methods based on photoemission spectroscopy, which we apply to a variety of samples ranging from single layers to full devices. The aim of the present work is twofold: first, we attempt to identify the efficiency limiting mechanisms in the different device stacks, and also, the strengths and weaknesses of the different electron transport layers (ETLs) and hole transport

J. Siekmann, S. Akel, B. Klingebiel, U. Rau, T. Kirchartz  
IEK5-Photovoltaik  
Forschungszentrum Jülich GmbH  
Wilhelm-Johnen-Straße  
52428 Jülich, Germany  
E-mail: t.kirchartz@fz-juelich.de

A. Kulkarni, M. Saliba  
Helmholtz Young Investigator Group FRONTRUNNER  
IEK5-Photovoltaik  
Forschungszentrum Jülich, 52425 Jülich, Germany  
E-mail: a.kulkarni@fz-juelich.de

M. Saliba  
Institute for Photovoltaics  
University of Stuttgart  
Pfaffenwaldring 47, 70569 Stuttgart, Germany

T. Kirchartz  
Faculty of Engineering and CENIDE  
University of Duisburg-Essen  
Carl-Benz-Str. 199, 47057 Duisburg, Germany

 The ORCID identification number(s) for the author(s) of this article can be found under <https://doi.org/10.1002/aenm.202300448>

© 2023 The Authors. Advanced Energy Materials published by Wiley-VCH GmbH. This is an open access article under the terms of the Creative Commons Attribution License, which permits use, distribution and reproduction in any medium, provided the original work is properly cited.

DOI: 10.1002/aenm.202300448

layers (HTLs) in combination with our specific perovskite layer. Second, we want to study the problem from the point of view of method development and method comparison. Hence, we focus on the problems or challenges in the analysis of different characterization methods, as well as on insights that can be obtained by analyzing different experiments in combination.

A crucial requirement for identifying suitable ETLs and HTLs for a given perovskite absorber layer is the band alignment at the interfaces toward the transport layers as well as the resulting band diagram. The band alignment is often determined by ultraviolet photoelectron spectroscopy (UPS).<sup>[17]</sup> The correct quantification of the valence band offset for halide perovskite layers is still an ongoing discussion.<sup>[18–20]</sup> In this work, we show the differences among the three methods for the determination of the valence band edge, and discuss the relationship between the observed energy levels and the predicted performance of a device using numerical simulations of current–voltage curves. To complement and compare the UPS data, we used space-charge-limited current (SCLC) measurements on single-carrier devices to gain insights into the band alignment between the perovskite and ETL. We find that both the band offset and the electron mobility in the transport layer change the ratio between the forward and reverse current density.

In addition to a suitable band offset, the transport layers should also feature low series resistances and minimize losses due to non-radiative recombination in the cell. We determined the series resistance by comparing the dark and illuminated current–voltage curves of the full devices.<sup>[12,21,22]</sup> Poor CTLs can minimize the fill factor (*FF*) of a cell. This can be attributed to the high series resistance or an ideality factor  $n_{id} > 1$ . We quantify both types of losses for solar cells with varying HTLs and ETLs and find that the loss in *FF* due to a high series resistance can occur due to poor HTL and ETL. The loss due to non-ideal diode behavior appears to be not as strongly influenced by the transport layers.

While there are relatively simple approaches to quantify recombination losses at open circuit in layers, layer stacks, and full devices, it is currently quite difficult to study the effect of transport layers on collection losses as well as resistive effects. Furthermore, gaining deep insights into recombination dynamics at interfaces is highly challenging because of the superposition of different effects that modify transient or frequency-domain experiments of layer stacks or full devices. Here, we overcome these challenges by combining several measurement methods. First, we use the combination of voltage-dependent photoluminescence (PL)<sup>[23–26]</sup> and transient PL<sup>[27]</sup> that provides information about charge carrier extraction. In the case of transient PL with contact layers, there is no clear way to tell whether a fast decay time is due to good extraction or high recombination.<sup>[27]</sup> However, a consistency check with the voltage-dependent PL shows that the fast decay is due to good extraction. Last, we investigate non-radiative recombination by combining steady-state PL and transient PL. Through the comparison between steady-state and transient photoluminescence, we can show that the longer lifetime of the transient PL (as compared to the steady-state PL) results from the de-trapping of charges that takes place at long times.

Our results highlight the importance of the critical analysis of different characterization methods that are used to gain insights into the properties of CTLs. By showing a broad range of charac-

terization methods, we provide tools to the community to select the appropriate CTL for their perovskite instead of testing various ETLs and HTLs.

## 2. Results

To investigate the influence of different charge transport layers on the performance of perovskite solar cells, we employ four different HTLs and three different ETLs. For HTLs, poly[bis(4-phenyl)(2,4,6-trimethylphenyl)amine] (PTAA) and carbazole-based self-assembled monolayers (SAMs) with phosphonic acid anchoring groups such as [2-(9H-Carbazol-9-yl)ethyl]phosphonic acid (2-PACz), [2-(3,6-Dimethoxy-9H-carbazol-9-yl)ethyl]phosphonic acid (MeO-2PACz), and (4-(3,6-Dimethyl-9H-carbazol-9-yl)butyl)phosphonic acid (Me-4PACz) were deposited, while C<sub>60</sub> fullerene and other fullerene derivatives such as [6,6]-phenyl-C<sub>61</sub>-butyric acid methyl ester (PCBM) and C<sub>60</sub>-fused *N*-Methylpyrrolidine-m-C<sub>12</sub>-phenyl (CMC) were deposited as ETLs. A triple cation (Cs<sub>0.05</sub>(FA<sub>0.83</sub>MA<sub>0.17</sub>)<sub>0.95</sub>Pb(I<sub>0.83</sub>Br<sub>0.17</sub>)<sub>3</sub>) perovskite with a bandgap ( $E_g$ ) of 1.62 eV, deposited using perovskite ink-substrate interaction strategy,<sup>[28]</sup> was sandwiched in between the HTL and ETL. It is important to note that the aim of the present work is not to employ different combinations of HTLs and ETLs and report the best device efficiency but rather to investigate the influence of different electron and hole transport layers on the experimentally accessible properties of interfaces, recombination, charge extraction, and device performance. To limit the range of options, C<sub>60</sub> and Me-4PACz were maintained as the default ETL and HTL, respectively, whereas the other transport layers were varied. The C<sub>60</sub> and Me-4PACz were maintained as default because they have been reported to demonstrate the highest efficiency in wide  $E_g$  single and silicon–perovskite tandem junction devices.<sup>[16]</sup>

### 2.1. Energy Level Alignment

The alignment of energy levels, that is, the conduction band edges of perovskite and ETLs, as well as the valence band edges of perovskite and HTLs, influence both recombination and extraction. We calculated the band offset, for example, at the perovskite–ETL interface using  $\Delta E_c = \chi_{ETL} - \chi_{perov}$ , where  $\chi$  represents the electron affinity of ETL ( $\chi_{ETL}$ ) and perovskite layer ( $\chi_{perov}$ ) (Figure S4, Supporting Information). Note that this equation only makes sense in the absence of interface dipoles caused by charged interfacial defects, which would lead to abrupt changes in the vacuum level. The optimum offset  $\Delta E_c$  is not necessarily the same for these two requirements. Given that interfaces break lattice periodicity; and hence, increase the likelihood of defects; device design in photovoltaics, in general, aims to minimize the density of electrons and holes that face each other across an interface. The exceptions to the above rule are recombination junctions (e.g., HTL to ITO), where hole conduction switches to electron conduction, and interface recombination is the desired event necessary for efficient current flow.

For a given voltage, the densities of electrons and holes facing each other across an interface between the absorber and the ETL will increase when the interfacial band gap  $E_{int} = E_g - \Delta E_c$

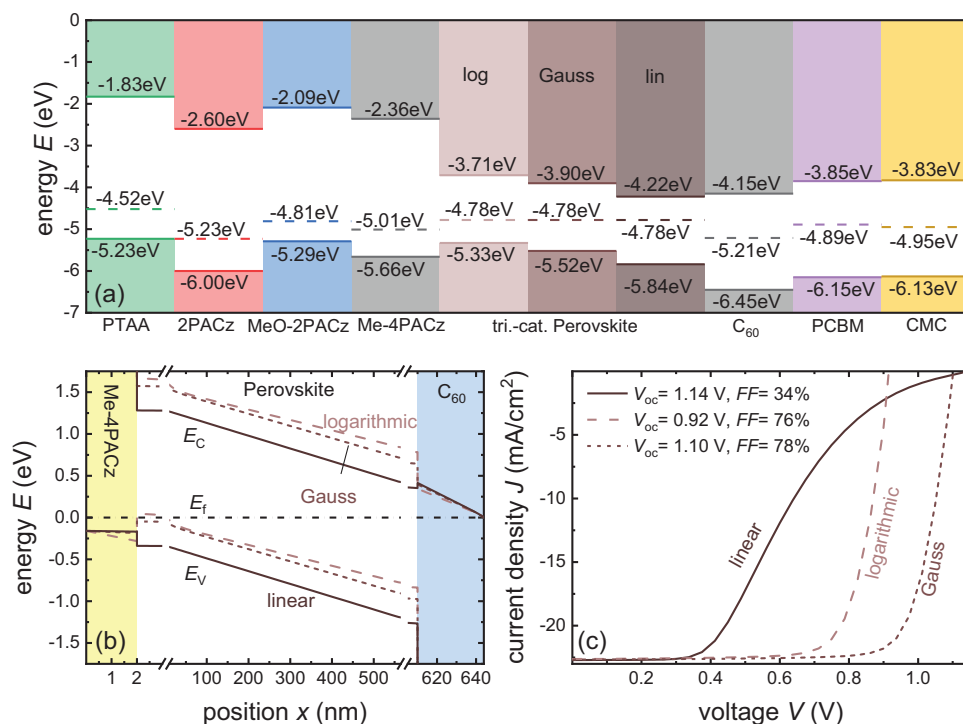


**Figure 1.** a) Schematic of the energy levels for different HTLs, perovskite on Me-4PACz, and different ETLs deposited on top of the perovskite. We evaluate the UPS measurement in three different ways, labeled logarithmic, Gauss, and linear. Each method leads to a different valence-band offset. b) Simulated band diagram of a cell with Me-4PACz as HTL and C<sub>60</sub> as ETL. The three different UPS methods: linear (solid line), logarithmic (dashed line), and Gauss (dotted line) lead to different possible band offsets between the CTLs and the perovskite. c) The current–voltage curve for the three different band diagrams; the linear method leads to a simulated  $V_{OC} = 1.14$  V but an S-shaped ( $FF = 34\%$ ) JV-curve; for the logarithmic method, the  $V_{OC} = 0.92$  V and  $FF = 76\%$ , and the Gauss method leads to the best cell with  $V_{OC} = 1.10$  V and  $FF = 78\%$ .

is lowered or the conduction band offset  $\Delta E_c$  is increased. Thus, to minimize recombination, the interfacial band gap at the perovskite–ETL interface should ideally be identical or even higher than the bulk band gap  $E_g$  of the absorber, implying that the band offset would be zero or even positive (forming a barrier for extraction).<sup>[29–31]</sup> In contrast, for efficient charge extraction at a short circuit, a higher value of  $\Delta E_c$  would be acceptable<sup>[31]</sup> as long as  $\Delta E_c$  does not become negative, that is, there is no barrier for electron extraction. The typical method to study the alignment of energy levels is ultraviolet photoelectron spectroscopy (UPS), which can be performed on different layer stacks. While the work function can be unambiguously determined from a UPS spectrum by measuring the position of the cutoff—that is the end of the spectrum at low kinetic photoelectron energy,<sup>[32]</sup> the determination of the valence band edge of halide perovskites is plagued by the difficulty of precisely pinpointing the high energy end of the spectrum because the photo electron count rate continuously decreases without a clear visible edge.<sup>[18]</sup> The electron affinity cannot be determined directly from UPS but can be obtained by adding the optical band gap of the material to the valence band edge. Thus, it faces the same or even more uncertainties as the valence-band edge.

**Figure 1a** shows the conduction band minimum (CBM), Fermi energy, and valence band maxima (VBM) at a vacuum energy  $E_{vac} = 0$  eV for different possible components of a p–i–n solar cell. For both different HTLs and ETLs, the valence band edge can be determined by a linear fit as explained in the Supporting Infor-

mation. For the conduction band edge, band gaps from the literature are assumed. For the HTLs, that is, PTAA and SAMs, the following band gaps are assumed: The band gaps of  $E_g = 3.4$  eV (PTAA),  $E_g = 3.2$  eV (MeO-2PACz),  $E_g = 3.4$  eV (2PACz),<sup>[8]</sup> and of  $E_g = 3.3$  eV (Me-4PACz) were adopted from references.<sup>[8,16]</sup> For the HTL, the ionization energy (represented by  $E_i = E_{vac} - E_v$ ) is the decisive parameter for carrier transport from the perovskite to the HTL. PTAA shows the lowest value of  $E_i$  while 2PACz shows the highest  $E_i$ . The electron affinity of an ETL is important for electron transport. For all three ETLs, a band gap of  $E_g = 2.3$  eV is assumed, resulting in C<sub>60</sub> having the largest electron affinity and CMC having a slightly smaller affinity than PCBM.

The band positions of the perovskite are decisive for the energy-level alignment and final band diagram. In contrast to the CTLs, there is no conclusive agreement on the optimal evaluation of the measurement data for the determination of the valence band edge according to the UPS. At least three approaches have been proposed in the literature: i) The linear evaluation developed by Kraut et al.<sup>[33]</sup> for crystalline semiconductors, used by us for the evaluation of the CTLs, ii) the evaluation via a logarithmic scale,<sup>[19]</sup> and iii) the fitting of a Gaussian function<sup>[18]</sup> to the valence band edge.

In a recent publication, Menzel et al.<sup>[34]</sup> presented a fourth fitting method using a more complex fit function based on a polylog function. This was used to fit the VBM spectra measured by a variant of photoelectron spectroscopy called constant final state yield spectroscopy (CFSYS), which yields a much higher dynamic

range and a different shape for the VBM spectra. Although this function could, in principle, be used to fit UPS spectra—owing to the higher noise level of UPS—this results in less stable fits and larger ionization energies, exceeding even the results of the linear evaluation. Even though these results could be corrected using extra parameters determined by CSFYS, we believe that the least complex fit model, which results in a good fit of the spectral data, should be used. As the classical linear evaluation fails for the perovskite spectra, this would be a Gaussian fit, as demonstrated by Endres et al.<sup>[18]</sup>

The application of the three valence band evaluation methods to perovskite samples is shown in Figure S1, Supporting Information. Figure 1b shows the simulated<sup>[35]</sup> band diagram, and Figure 1c shows the current–density–voltage (*JV*) curve of a cell with Me-4PACz as the HTL and C<sub>60</sub> as the ETL for all three evaluation methods. First, we consider the linear (solid line) evaluation. As the linear evaluation is not sensitive to the background, the measurements can be compared well with each other, implying that it is well suited to study trends. However, because the valence band edge in perovskite is not very steep, the linear method leads to an overestimation of the ionization energy.<sup>[19]</sup> This results in a significant electron extraction barrier of  $\Delta E_c = \chi_{\text{ETL}} - \chi_{\text{perov}} = -62$  meV between the conduction band of the perovskite and C<sub>60</sub>. For the other fullerenes, this barrier is even higher (Figure S5a, Supporting Information). The Me-4PACz/perovskite interface shows a band offset of  $\Delta E_v = E_i^{\text{perov}} - E_i^{\text{HTL}} = 170$  meV. The simulated *JV* curve for the linear evaluation method (solid line) and C<sub>60</sub> as ETL show an S-shape and a poor *FF*. The second method we consider determines the valence band edge on a semi-logarithmic scale (dashed line) from the intersection between the background and the valence band edge. On the logarithmic axis, the result is significantly more dependent on the background than when using the linear method. As the background depends on the measurement conditions, the comparability between different measurements analyzed with the logarithmic method is not as good as with the linear evaluation. However, the ionization energies are smaller and do not result in electron extraction barriers in the band diagram, leading to more realistic *JV* simulations (dashed line) with an open-circuit voltage  $V_{\text{OC}} = 0.92$  V and *FF* = 76%. The HTL/perovskite interface shows an extraction barrier for holes of  $\Delta E_v = -330$  meV. We enable tunneling through thin barriers in the drift–diffusion simulation as we assume that this is a realistic transport scenario for the monolayer-based HTLs. This assumption causes only an increase in  $V_{\text{OC}}$  for the simulated *JV* curve of Me-4PACz to MeO-2PACz; although, there is a hole barrier for Me-4PACz ( $\Delta E_v = -330$  meV) and just an offset of  $\Delta E_v = 70$  meV for MeO-2PACz. Despite tunneling, the barrier height seems to prevent the simulation for 2PACz from converging for higher voltages. Further descriptions of the band diagrams and *JV* curves are given in Chapters S2.1.1 and S2.1.2, Supporting Information. As an alternative to both methods, a Gaussian function can be fitted to the leading edge of the UPS spectra and the VBM position is determined only by the position and standard deviation  $\sigma$  of the Gaussian function (dotted line). In contrast to the two aforementioned methods, the problematic intersection with the background level (which is influenced by the measurement conditions) is not used. However, with the Gaussian fit, the problem remains as to where to define the exact posi-

tion of the VBM. Endres et al.<sup>[18]</sup> compared DFT simulations with experimental UPS and IPES data and suggested a correction factor of  $2.9 \times \sigma$  if the Gaussian fit was used, where  $\sigma$  is the standard deviation of the Gaussian. The last method results in an ionization energy that is between those of the linear and logarithmic methods and is not sensitive to the background. The simulated *JV* curve (dotted line) with  $V_{\text{OC}} = 1.10$  V and *FF* = 78% fits best to the measured samples. In conclusion, we note that the translation of photoemission spectroscopy data into an approximately realistic device model strongly depends on the choice of energy levels, even if we assume that the problematic interface is only toward the ETL and the monolayer-based HTLs can extract holes by tunneling through a barrier.

## 2.2. Single Carrier Devices

Measuring *JV* curves of single-carrier devices is a highly popular method in perovskite photovoltaics that is regularly used to either determine mobilities<sup>[36,37]</sup> or trap densities.<sup>[38,39]</sup> Furthermore, it could be used in general to identify differences in injection barriers;<sup>[40]</sup> although, the method has so far been rarely applied. In single-carrier devices, recombination is of no relevance as only the transport of the majority carriers is required to obtain current flow. This transport of majority carriers is non-ohmic, as long as the semiconductor is sufficiently intrinsic to avoid the dark conductivity of the semiconductor to dominate transport. In the absence of any considerable dark conductivity but in the presence of two contacts that efficiently inject and extract one type of charge carrier, the mobility of the semiconductor, the injection barrier, and the amount of space charge dominate and limit the amount of current that can flow through the semiconductor at a given voltage. In the absence of contact- or defect-related effects, the space charge of injected carriers limits the current flow, and one observes space-charge limited conduction, which allows the detection of mobilities.<sup>[36,41]</sup> If the space charge of charged defects has a significant impact on the total space charge, one may observe the so-called trap-limited current<sup>[38,42]</sup> that allows the determination of defect densities. However, neither situation can be easily achieved in halide perovskites. Instead, the current is typically heavily affected by space charge induced by mobile ions,<sup>[43,44]</sup> that is, a special case of charged defects, and by the injection barriers at either contact. Thus, the analysis of single-carrier *JV* curves requires a critical assessment of the assumptions of the used analysis approaches. Important insights are obtained from the comparison of all four branches of the *JV*-curves,<sup>[45]</sup> that is, to compare both the scanning direction (high to low voltages or vice versa) and the polarity (e.g., injection of electrons from one contact or from the other).

We fabricated electron-only devices by deposition of SnO<sub>2</sub> on ITO with atomic layer deposition followed by spin coating the perovskite and evaporation of C<sub>60</sub> fullerene. BCP and Ag were deposited as back contacts. The devices were measured in the dark from  $-3$  to  $3$  V (Figure S8, Supporting Information, solid line) and from  $3$  to  $-3$  V (Figure S8, Supporting Information, dashed line).

Figure 2a shows the dark *JV* curve of the electron-only device with C<sub>60</sub> as ETL (squares), measured from  $-3$  to  $3$  V on a double logarithmic plot. The lower branch is the current for



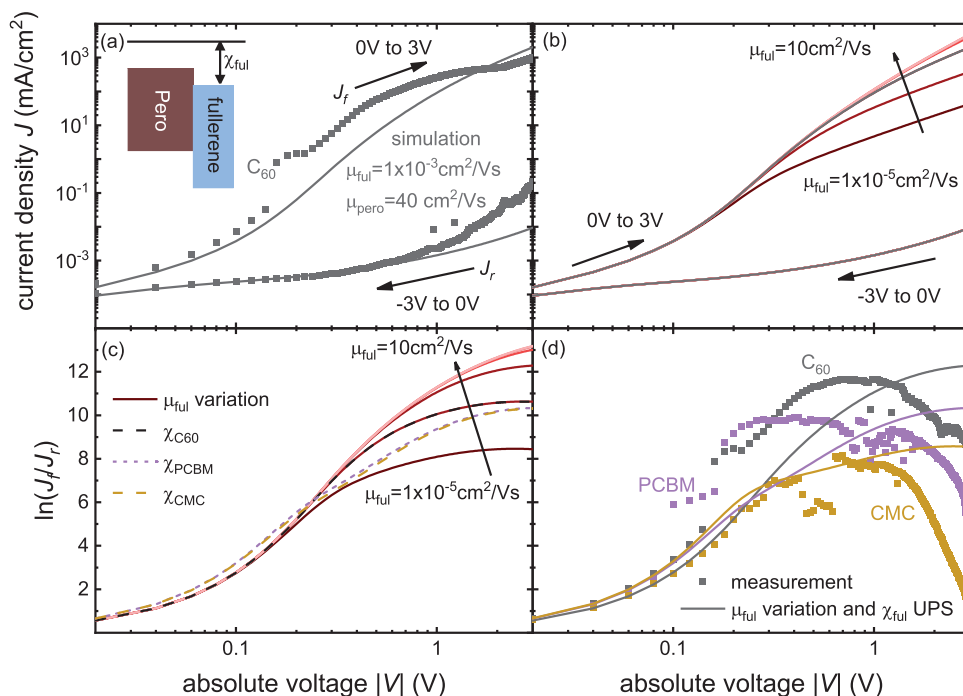


**Figure 2.** a) Dark JV-curves of the electron-only device with  $C_{60}$  as ETL (squares) and the corresponding simulations using ASA (solid lines). The parameters are listed in Table S4, Supporting Information. The lower branch with the arrow to the left is the measurement/simulation from  $-3$  to  $0$  V (reverse current  $J_r$ ) and the upper branch with the arrow to the right part determines the measurement/simulation from  $0$  to  $3$  V (forward current  $J_f$ ). b) ASA simulations for an electron-only device with different electron mobility in the fullerene ( $1 \times 10^{-5}$  to  $10 \text{ cm}^2 \text{ V}^{-1} \text{ s}^{-1}$ ). The curve does not change from  $-3$  to  $0$  V (lower branch) and increases for higher mobilities with increasing mobility in the fullerene. c) Logarithmic ratio of forward  $J_f$  ( $0$  to  $3$  V) and reverse  $J_r$  ( $-3$  to  $0$  V) current with the different fullerene mobilities used in (b) (solid lines) and with the same mobility but the electron affinity of the three fullerenes measured with UPS (dashed line). d) Logarithmic  $J_f/J_r$  ratio calculated from the measurements of electron-only devices with different fullerenes (squares). The combination of different mobilities for each fullerene and the corresponding UPS electron affinities (lines) lead to  $J_f/J_r$  ratios with a maximum similar to the measured curves.

negative (reverse) voltages and the upper branch corresponds to positive (forward) voltages. The simplest method to derive the mobility from the curve would be the use of the Mott-Gurney equation (Equation (S1), Supporting Information) applied to the drift-limited region with a slope close to two.<sup>[46]</sup> The linear fit to the region would lead to an apparent electron mobility  $\mu_{\text{app}} \approx 0.02 \text{ cm}^2 \text{ V}^{-1} \text{ s}^{-1}$ . However, the Mott-Gurney law is only valid under several conditions.<sup>[36]</sup> One condition is a strictly drift-controlled current, where diffusion terms can be neglected. This condition is violated by asymmetric injection barriers and is potentially due to the existence of charged (and mobile) defects in the device. The asymmetric contacts can be deduced from the difference in current for negative and positive voltage scans.<sup>[40,46]</sup> Furthermore, the Mott-Gurney law considers only one semiconductor sandwiched between two highly conductive contacts. Only the material between the contacts limits the electron mobility in the device. However, we used a device stack with perovskite and fullerenes, which are known to have low conductivities.<sup>[9]</sup> To investigate the impact of low transport layer mobilities, we performed simulations by varying the electron mobilities in fullerene and perovskite using the drift-diffusion simulation tool ASA.<sup>[47,48]</sup> The simulated JV curves for electron-only devices with a variable electron mobility in the fullerenes and in the perovskite are depicted in Figure 2b; Figure S9, Supporting Information, respectively. The mobility  $\mu_{\text{ful}}$  varies from  $10^{-5}$  to

$10 \text{ cm}^2 \text{ V}^{-1} \text{ s}^{-1}$ . The lower branch does not change but the upper branch, that is, the drift-dominated regime increases with higher mobility in the fullerene and starts to saturate for mobilities between  $1$  and  $10 \text{ cm}^2 \text{ V}^{-1} \text{ s}^{-1}$ . This indicates that the current is limited by the layer with the lowest mobility which is either the perovskite or the fullerene. The gray line in Figure 2a is the fitted JV-curve from the ASA simulations, where we used a mobility in the perovskite of  $\mu_{\text{pero}} = 40 \text{ cm}^2 \text{ V}^{-1} \text{ s}^{-1}$  while the mobility in the fullerene was  $\mu_{C60} = 1 \times 10^{-3} \text{ cm}^2 \text{ V}^{-1} \text{ s}^{-1}$ . The mobility for perovskite fits to previously measured mobilities in perovskite.<sup>[49-51]</sup> The fullerene mobility is low for  $C_{60}$  but in the range of other fullerenes.<sup>[9,52]</sup> Figure S8, Supporting Information, shows the electron-only devices containing the three different fullerenes. All devices have asymmetric injection barriers as the curve from  $-3$  to  $0$  V (arrow to the left) produces significantly less current than the measurement from  $0$  to  $3$  V (arrow to the right).

In an electron-only device with one layer between two asymmetric ohmic contacts, it is possible to calculate the built-in voltage for  $|V| \gg V_{\text{bi}}$ <sup>[40]</sup> via

$$V_{\text{bi}} = \frac{kT}{q} \ln \left( \frac{8}{9} \frac{q N_c d^2}{\epsilon_r \epsilon_0} \frac{J_f}{J_r} \frac{1}{V} \right) \quad (1)$$

which is independent of the mobility of the layer. The built-in voltage is a function of the temperature  $T$ , the Boltzmann

constant  $k$ , the thickness  $d$ , the density of states in the conduction band  $N_C$ , the dielectric constant  $\epsilon_r$ , and the ratio of the forward  $J_f$  (0 to 3 V) and reverse  $J_r$  (−3 to 0 V) current. For a hole-only device, the effective density of states of the valence band has to be used. Note that Equation (1) is derived from the ratio of the  $V_{bi}$ -corrected Mott–Gurney law to an analytical description of the current based on diffusion against the (assumed to be constant) electric field created by the  $V_{bi}$ .<sup>[53]</sup> The conditions that must be met for Equation (1) to be valid are  $V_{bi} \gg kT/q$ , absence of recombination, a constant electric field for the case of  $J_r$  (but not  $J_f$ ), constant mobility, and permittivity.

According to Equation (1), the built-in voltage depends on the material properties and the logarithmic ratio of the forward and reverse currents. However, in Figure 2b, we see that this ratio depends heavily on the mobility of the fullerene, which is not factored into the equation. The solid lines in Figure 2c show the logarithmic  $J_f/J_r$  values of the simulated curves for different fullerene mobilities. As we have two layers, that is, perovskite and fullerene, the ratio depends not only on the barrier created by the built-in voltage but also on the barrier created by the offset between perovskite and fullerene. Figure 2c shows the  $J_f/J_r$  ratios for the three electron affinities obtained from UPS measurements (dashed lines). The ratio is the highest for the electron affinity of  $C_{60}$  and nearly equal for PCBM and CMC. However, from Figure 2b, it is clear that the electron mobility of the fullerene has a larger influence on the  $J_f/J_r$  ratio than the electron affinity. Figure 2d shows the current ratio calculated from the three electron-only devices with different fullerenes (squares) and calculated for simulations with the electron affinity from the UPS and mobilities selected such that the maximum of the simulated ratio is close to the measurement results. Owing to the large influence of electron mobility in the fullerene, the ratio cannot be used to obtain an insight into the band alignment of the perovskite and the different fullerenes. However, the ratio between the forward and reverse currents may help estimate the relevant mobility in the CTL.

### 2.3. Cell Performance

In the following, we present the effects of different HTLs and ETLs on the performance of the perovskite solar cells. **Figure 3a,b** shows the best (highest efficiency) performing JV curves in the forward (dashed lines) and backward scans of devices employing different combinations of HTLs and ETLs, respectively. We note that all the device stack layers are fully optimized. The obtained device efficiencies, with different HTLs and  $C_{60}$  as the ETL, showed one of the highest efficiencies and were in the same range reported in the literature. The JV curve (black line) of the Me-4PACz/  $CS_{0.05}(FA_{0.83}MA_{0.17})_{0.95}Pb(I_{0.83}Br_{0.17})_3$  perovskite/ $C_{60}$  based device is shown as a reference in both figures. All cells were stabilized with several JV measurements under LED illumination (Figure S13a, Supporting Information). As indicated by maximum power point tracking (MPPT) (Figure S13b, Supporting Information), for an example device ( $V_{max} = 0.98$  V) showing an efficiency of 19.6% under one Sun illumination and 19.5% with MPP tracking, the cells are stable for several minutes. Figure 3c–f shows the box plots highlighting the influence of CTLs employed on the device characteristics of perovskite solar cells.

Devices employing different SAMs (Me-4PACz, 2PACz, and MeO-2PACz) with a  $C_{60}$  ETL showed similar device performance, whereas Me-4PACz-based cells showed slightly better efficiency owing to a higher  $FF$  compared to MeO-2PACz and 2PACz as HTL-based cells. The PTAA-based cells showed the lowest device performance, with all device parameters ( $J_{SC}$ ,  $V_{OC}$ , and  $FF$ ) being lower than those of the solar cells employing SAMs. The PTAA cell with the highest efficiency (shown in Figure 3a) is the only device with such a high  $FF$ .

When changing the ETLs while keeping the Me-4PACz HTL constant, we observed that the device with  $C_{60}$  as the ETL exhibited the highest efficiency owing to the high  $FF$  compared to the case with PCBM and CMC as ETLs. We observed no significant difference in cell performance when  $C_{60}$  was replaced with PCBM, whereas in the case of CMC-based cells, the device showed low  $J_{SC}$  and  $FF$ . In contrast to PCBM, CMC has solubility issues and tends to crystallize rapidly during spin coating, which could be the reason for the reduced  $J_{SC}$  and  $FF$  values. However, it was interesting to observe that by replacing  $C_{60}$  with PCBM and CMC, the  $V_{OC}$  of the devices improved. Thus, the ETL variation shows an anti-correlation between the recombination at open circuit and the recombination and resistive effects that occur during transport (i.e., voltages below  $V_{OC}$ ). The key values for the best-performing devices in all cases and the median cells are listed in Table S5, Supporting Information.

### 2.4. Charge Transport

One selection criterion for CTLs is efficient charge extraction.<sup>[54]</sup> This means that the film should be as conductive as possible and should not present a barrier for extraction, as discussed in Section 2.2. Therefore, one way to determine the quality of CTLs is to compare the series resistances ( $R_s$ ) of cells comprising different CTLs. The  $R_s$  is traditionally understood as an ohmic or nearly ohmic resistance in series with the diode (i.e., the non-linear, rectifying part of the solar cell). However, as resistive effects can also be non-ohmic (i.e., non-linear with voltage), it is often not possible to determine a single value for  $R_s$ . Furthermore,  $R_s$  always depend on the method used to determine its value as there is no universal approach to quantify resistive losses. This section considers the  $R_s$  as a function of voltage (or current) obtained by comparing dark and light JV curves and discusses its influence on the  $FF$ .<sup>[9,12]</sup> Furthermore, we consider charge extraction through the ETL by voltage-dependent PL measurements and compare the results with the initial decay of the PL transients.

**Figure 4a,b** shows the dark  $JV_d$  curves (dashed line) and shifted illuminated  $JV_l$  curves (solid line) on a semilogarithmic scale for devices with different HTLs and ETLs, respectively. In the case of the illuminated JV curves (Figure 4b), the region with a moderate slope at low voltages exhibited a weak voltage-dependent recombination current. This so-called photo-shunt is an indication of poor charge-carrier extraction at low voltages, most likely caused by the finite conductivity of the undoped transport layers.<sup>[12]</sup> A quantitative evaluation of the shunt is not easy; however, by comparing the currents at low voltages, as shown in Figure 4a, it becomes clear that there is no significant difference in charge transport for different HTLs. For the ETLs (Figure 4b), CMC has the highest photo-shunt indicating a high carrier concentration

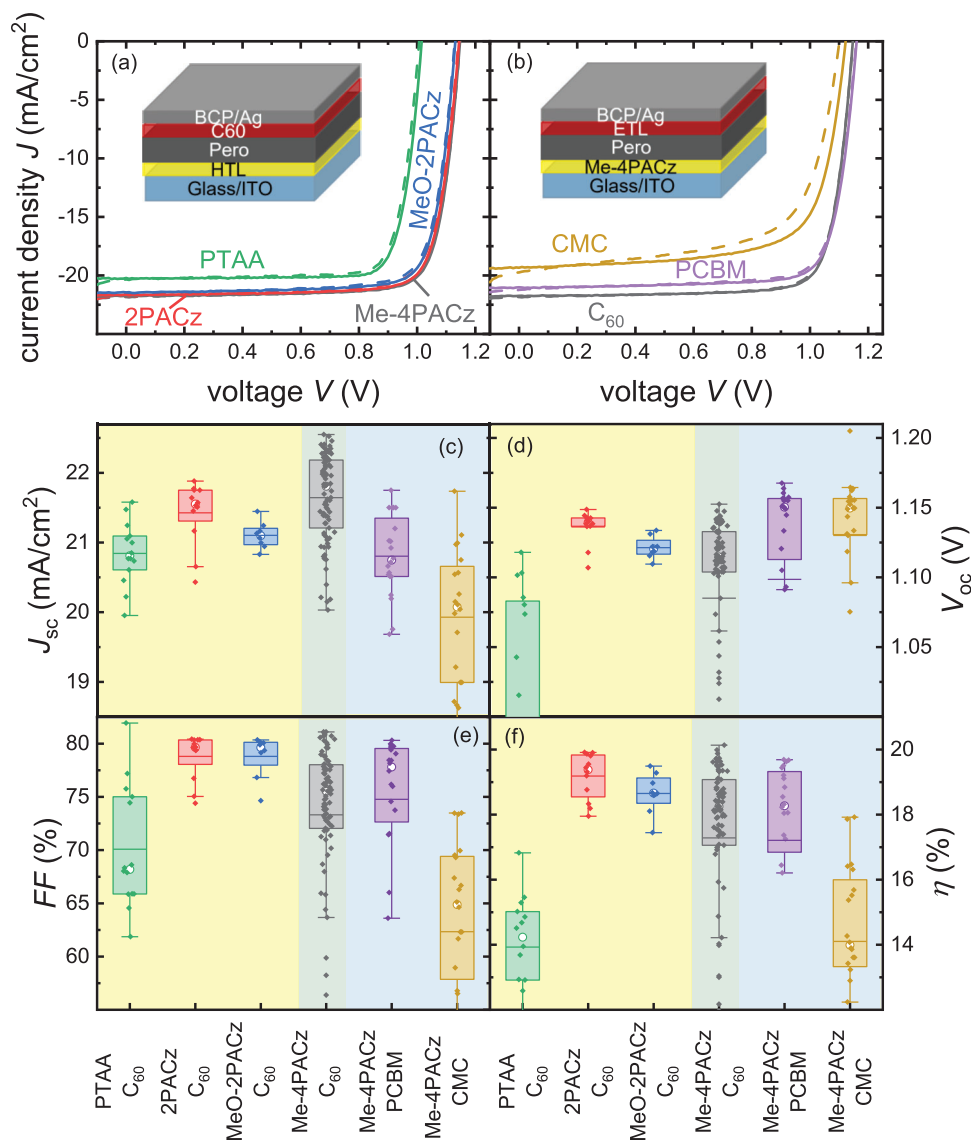


**Figure 3.** Illuminated  $JV$  curves measured using an AAA Sun simulator in the forward (dashed line) and backward (solid line) scan directions. a) Variation in HTLs with C<sub>60</sub> ETL as constant. b) Variation in ETLs by keeping Me-4PACz constant. c–f) Statistics of short-circuit current  $J_{sc}$  (c), open-circuit voltage  $V_{oc}$  (d), fill factor  $FF$  (e), and efficiency  $\eta$  for all the cases studied (f). The filled symbols represent the measured data, the box contains 50% of the data, the bars represent the mean values, and the circles represent the median values.

at short circuit and low forward bias caused by poor charge extraction. This finding is consistent with the reduced  $FF$  and  $J_{sc}$  values (Figure 3) of CMC-based devices. However, the statistical fluctuations of the CMC-based devices are rather high. The 50% range of the  $J_{sc}$  data starts from 19 mA cm<sup>−2</sup> and ends at 20.7 mA cm<sup>−2</sup>, and the  $FF$  ranges from 57.9% to 69.4%.

The series resistance can be determined in different ways, including by the difference formed by the illuminated, dark, or  $J_{sc} V_{oc}$  characteristic in the 4th quadrant (Section S2.4.3, Supporting Information).<sup>[12,21,22,55,56]</sup> Here, we have chosen to determine the series resistance by the difference between the dark and the illuminated  $JV$  curve because the asymptotic approximation of the illuminated  $JV$  curve and the  $J_{sc} V_{oc}$  curve causes the series resistance to approach zero for voltages around  $V_{oc}$  at one sun;

and for dark and  $J_{sc} V_{oc}$  curves, the same happens for medium voltages around the maximum power point (Figure S19, Supporting Information). Figure 4c,d shows the voltage-dependent  $R_s$  for the devices with different HTLs and ETLs, respectively. For lower voltages ( $V_d < 1.15$  V), the values of  $R_s$  are high mainly because of the increasing internal  $R_s$  in the cell. At higher voltages ( $V_d \geq 1.15$  V), the curves exhibit a flat region corresponding to the external  $R_s$ . The  $R_s$  for the PTAA-based cell (with C<sub>60</sub> as ETL) shows the highest external  $R_s$  of 15.3  $\Omega$ cm<sup>2</sup> in a voltage range of  $V_d \geq 1.15$  to  $\approx 1.3$  V, while the lowest  $R_s$  of 2.0  $\Omega$ cm<sup>2</sup> is observed in the same voltage range for the device with MeO-2PACz as HTL (with C<sub>60</sub> as ETL). Furthermore, among the various ETLs, the PCBM-based cell (with Me-4PACz SAM as the HTL) shows the lowest  $R_s$  of 2.0  $\Omega$ cm<sup>2</sup>. This suggests that both the ETL and

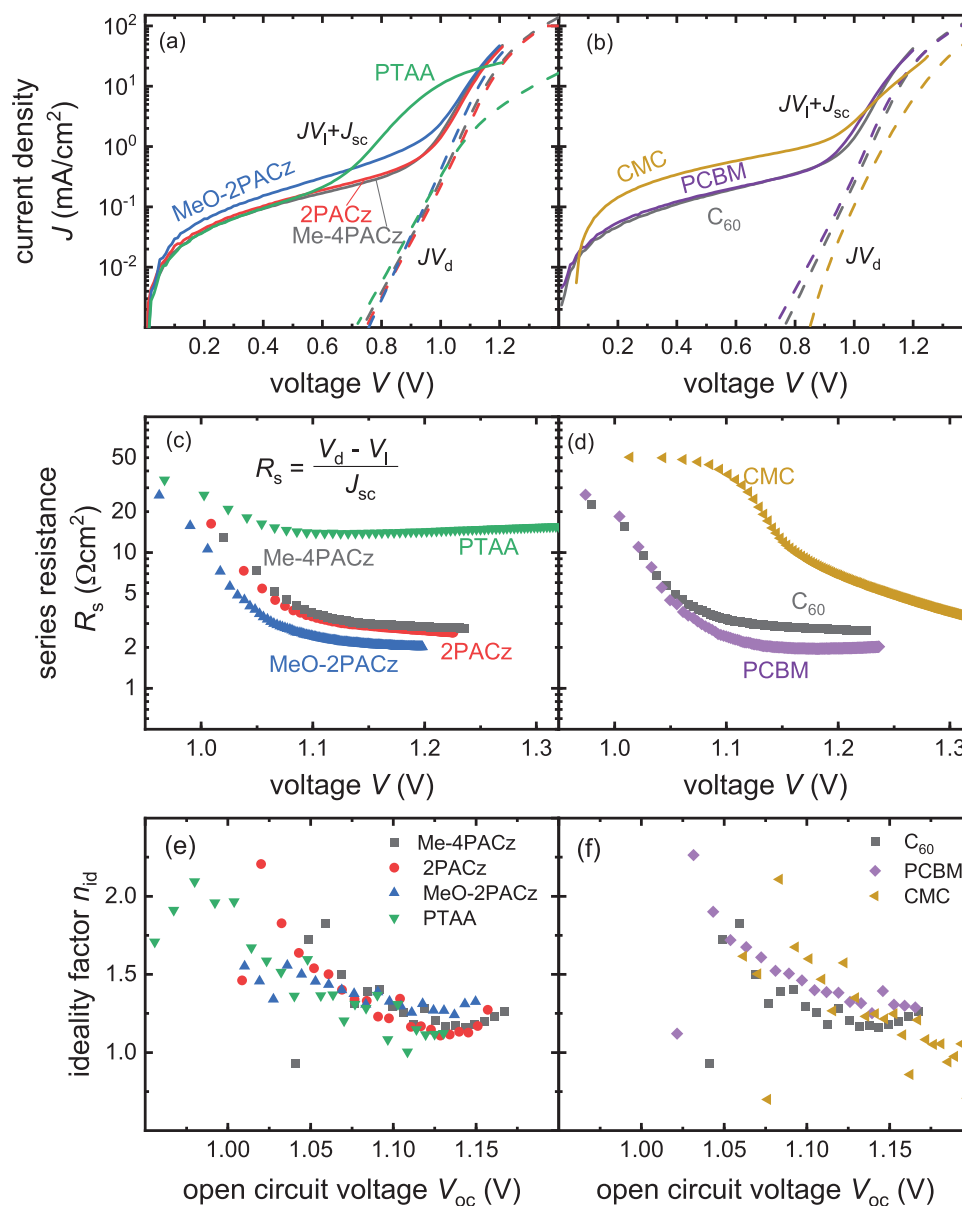


**Figure 4.** Dark (dashed line) and illuminated (solid line) JV curves plotted in the first quadrant. a) Devices with different HTLs and C<sub>60</sub> as the ETL and b) devices with Me-4PACz as the HTL and different ETLs. The Me-4PACz and C<sub>60</sub> curves are identical.  $R_s$  was calculated from the difference between the dark and illuminated JV curves.  $R_s$  calculated for devices c) with different HTLs and C<sub>60</sub> as the ETL and d) with different ETLs and Me-4PACz as the HTL. e,f) Ideality factor derived from Suns- $V_{oc}$  measurements.

HTL limit the  $R_s$  of the cell, and the choice of a suitable combination of CTLs can help to reduce  $R_s$  and improve the FF of the cell. To further confirm this conclusion, we fabricated a device with MeO-2PACz and PCBM as HTL and ETL, respectively, and the resultant perovskite device showed one of the highest efficiencies  $\eta = 21\%$  with an FF of  $\approx 83\%$ . The JV curve of the device is shown in Figure S15, Supporting Information. Figure 4e,f shows the voltage-dependent ideality factor for the cells with different CTLs. The ideality factor at high voltages is constant for a small range of voltages from 1.1 to 1.15 V. In this region, we calculate the cell ideality factor using the arithmetic mean. For CMC, two regions with nearly constant ideality factors can be found,

from 1.2 to 1.15 V and from 1.15 to 1.1 V, the ideality factor is  $n_{id} = 1.06$  and  $n_{id} = 1.37$ . For the other cells, the ideality factors lie between  $n_{id} = 1.13$  and  $n_{id} = 1.28$ . For the different HTLs, PTAA shows the lowest  $n_{id}$  while MeO-2PACz shows the highest. For different ETLs, the  $n_{id}$  of C<sub>60</sub> is lower than that of PCBM, and both are between the two ideality factors of the CMC. If we assume that some type of defect-assisted recombination is dominant in our devices, ideality factors would be close to 2 if two necessary conditions coincide: i) The concentrations of electrons and holes are similar ( $n \approx p$ ) and ii) the defect is between the two quasi-Fermi levels, that is, sufficiently deep.<sup>[57]</sup> All ideality factors are; however, close to  $n_{id} = 1$ , suggesting that one of the two



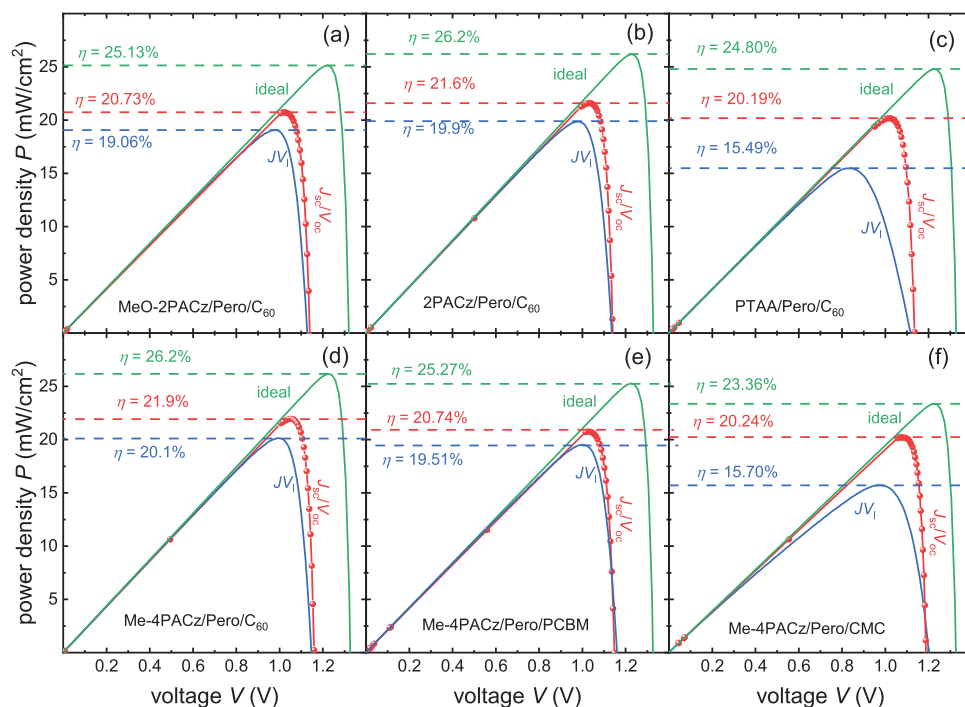


**Figure 5.** Power density of the illuminated cell (blue), reconstructed from the  $J_{SC}/V_{OC}$  curve (red) and ideal curve (green) for cells with different a–c) HTLs and d–f) ETLs. The dashed lines indicate the maximum power density, that is, the efficiency of the measured, series resistance-free, and ideal solar cells.

conditions mentioned above must be violated. Thus, recombination dominantly occurs in regions of the cell where the electron and hole densities are unequal, and/or the position of the most recombination-active defect within the band gap is far away from the mid gap (shallow defect).

To further investigate the influence of series resistance and ideality factor on the cell performance, we compare the power density of the illuminated  $JV_1$  curve (blue) and the reconstructed power density from  $J_{SC}/V_{OC}$  (red) (Figure 5) (see Paragraph S2.4.2, Supporting Information). By showing the power-density voltage curve rather than the  $JV$  curve, the efficiency of the cell can be easily read from the maximum of the curves. The difference in efficiency and  $FF$  between the illuminated  $JV_1$  curve and  $J_{SC}/V_{OC}$  curves is due to the absence of voltage losses over series resistances in the  $J_{SC}/V_{OC}$  measurement ( $\Delta FF_{R_s} = FF_{J_{SC}/V_{OC}} - FF_1$ ). In addition, we calculated the ideal  $JV$  curve using the measured  $J_{SC}$  and radiative  $V_{oc,rad} = 1.33$  V in the diode equation (Equation (S3), Supporting Information) with  $n_{id} = 1$  and  $R_s = 0$  (green). The radiative  $V_{oc,rad}$  is defined by ref. [58] and calculated using the external quantum efficiency as described by ref. [59]. The potential of the cell is shown by the use of the radiative  $V_{oc,rad}$ ; thus, different technologies or perovskites can be compared. The difference between the measured and  $V_{oc,rad}$  can be used to determine the magnitude of the non-radiative loss. Note that it is important to use  $V_{oc,rad}$  instead of the Shockley–Queisser  $V_{oc}$  to determine the ideal cell. This is because  $V_{oc,rad}$ , and not  $V_{oc,SQ}$  indicates the maximum possible  $V_{oc}$  of the cell. These can differ greatly due to non-ideal band structures, that is, broad band edges.<sup>[58]</sup> By comparing these ideal curves with the ones constructed from the  $J_{SC}/V_{OC}$  data ( $\Delta FF_{n_{id}} = FF_{ideal} - FF_{J_{SC}/V_{OC}}$ ), we

can determine the loss due to non-ideal diode behavior, that is,  $n_{id} \neq 1$ . From Figure 4, we can see that the loss due to the series resistance is highest for PTAA ( $\Delta FF_{R_s} = 19.0\%$ ) and CMC ( $\Delta FF_{R_s} = 20.4\%$ ). In addition to this, Figure 4 suggests that the loss due to  $R_s$  is low for the combination with PCBM ( $\Delta FF_{R_s} = 5.3\%$ ) and MeO-2PACz ( $\Delta FF_{R_s} = 6.2\%$ ). However, despite the higher  $R_s$ , the lowest loss occurs for Me-4PACz ( $\Delta FF_{R_s} = 4.8\%$ ). Next, we look at the loss due to  $n_{id} > 1$ . We observe the lowest loss for 2PACz ( $\Delta FF_{n_{id}} = 2.3\%$ ); the loss for CMC is low as well ( $\Delta FF_{n_{id}} = 2.9\%$ ), which is consistent with the high  $V_{OC}$  of the cell and the ideality factor close to  $n_{id} = 1$ . For all combinations, the  $FF$  loss arises either in equal parts from  $R_s$  and from non-ideal diode behavior, or predominantly because of the series resistance (especially for PTAA and CMC). All values are tabulated in Table 1. Figure S20, Supporting Information, shows the correlation between the series resistances and ideality factors and the respective losses in the  $FF$ . Notably, the accuracy of  $n_{id}$  determination is not very good because no clear plateau can be recognized. Therefore, no clear trend between the data can be recognized.

To study the losses in  $J_{SC}$  due to the non-ideal extraction of the photogenerated charge carriers by the CTLs, we measure the voltage-dependent photoluminescence  $PL(V)$ <sup>[23–26,60]</sup> for three perovskite solar cells of different ETLs ( $C_{60}$ , PCBM, and CMC). From the  $PL(V)$  measurement with the obtained  $J_{SC}$  and the ideality factor  $n_{id}$  for each device, the recombination current density ( $J_{rec}$ ) can be evaluated from<sup>[12]</sup>

$$J_{rec} = \frac{J_{sc} \phi(V)^{\frac{1}{n_{id}}}}{\phi_{oc}^{\frac{1}{n_{id}}} - \phi_{sc}^{\frac{1}{n_{id}}}} \quad (2)$$

**Table 1.** Fill factor from illuminated  $JV$  curve ( $FF_I$ ),  $J_{SC}/V_{OC}$  curve ( $FF_{J_{SC}/V_{OC}}$ ), and ideal  $JV$  curve with ideal fill factor ( $FF_{ideal}$ ). The loss due to  $R_s \neq 0$  is given by  $FF_{J_{SC}/V_{OC}} - FF_I = \Delta FF_{R_s}$  and the loss due to  $n_{id} \neq 1$  is given by  $FF_{ideal} - FF_{J_{SC}/V_{OC}} = \Delta FF_{n_{id}}$ .

Sample	$FF_I$ [%]	$FF_{J_{SC}/V_{OC}}$ [%]	$FF_{ideal}$ [%]	$\Delta FF_{R_s}$ [%]	$\Delta FF_{n_{id}}$ [%]
MeO-2PACz/Pero/ $C_{60}$	80.3	86.5	90.5	6.2	4.0
2PACz/Pero/ $C_{60}$	80.4	88.2	90.5	7.9	2.3
PTAA/Pero/ $C_{60}$	67.3	86.3	90.5	19.0	4.3
Me-4PACz/Pero/ $C_{60}$	80.7	85.6	90.5	4.8	5.0
Me-4PACz/Pero/PCBM	80.0	85.2	90.5	5.3	5.3
Me-4PACz/Pero/CMC	67.2	87.6	90.5	20.4	2.9

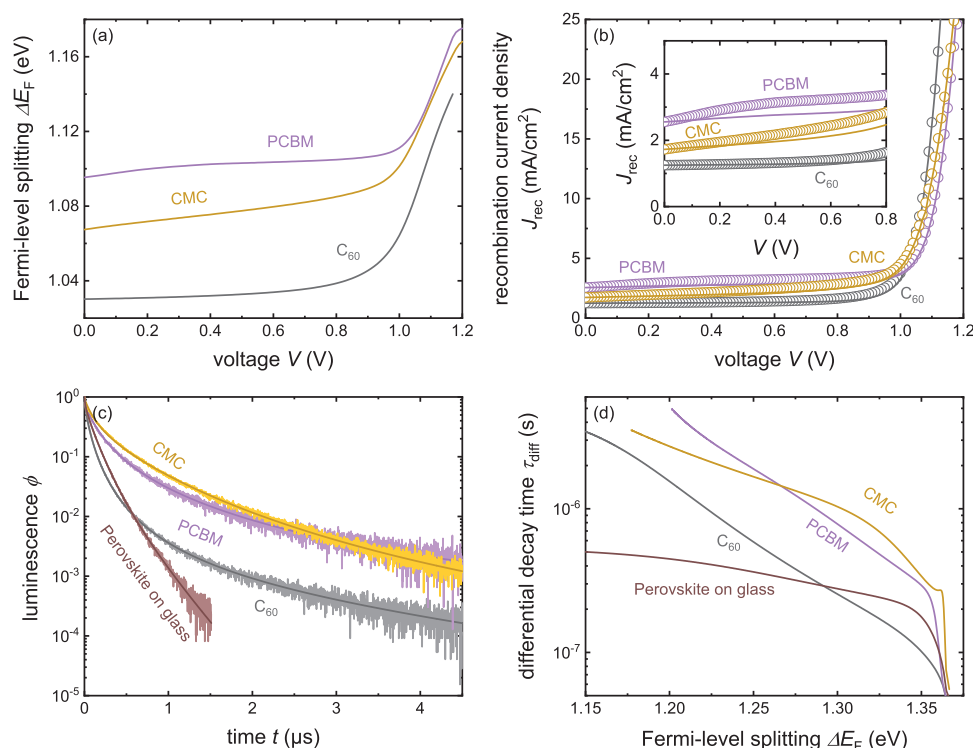


**Figure 6.** a) The Fermi-level splitting versus the external bias obtained from the voltage-dependent photoluminescence measurement for three perovskite solar cells using  $C_{60}$ , PCBM, or CMC as ETL. b) The recombination current density as a function of the external voltage was calculated from the PL(V) data using Equation (2)<sup>[12]</sup> (open circles) with an ideality factor of 1.2 for  $C_{60}$ , 1.33 for PCBM, and 1.36 for CMC, or from the light  $JV$ -curve that was measured using the PL(V) setup and the maximum possible photocurrent for each device (solid lines) such that  $J_{rec} = J_{light} + J_{ph,max}$ . A zoom in the region of SC and low forward bias is shown;  $J_{rec}$  at SC fit perfectly from both the PL(V) and the upshift of the light  $JV$ -curve by  $J_{sc}$  for the three devices. c) The tr-PL-decay measured with  $258.2 \text{ nJ cm}^{-2}$  laser intensity of the layer stack Me-4PACz/Pero/ETL for varying ETLs and as reference of the perovskite on glass. A rational function was fitted to the background-corrected decay data of each curve. d) Differential decay times calculated from the fitted tr-PL data as a function of Fermi-level splitting.

where  $\phi(V)$  is the voltage-dependent luminescence intensity,  $\phi_{oc}$  is the luminescence at open circuit, and  $\phi_{sc}$  is the luminescence at short circuit.

**Figure 6a** shows the quasi-Fermi level splitting ( $\Delta E_F$ ) as a function of external voltage for three cells with  $C_{60}$ , PCBM, and CMC that we extracted from the photoluminescence intensity. Note that these cells are not identical to those discussed in Figures 4 and 5 but were made using the same recipes. If carrier extraction is efficient, the  $\Delta E_F$  at short circuit should be as small as possible. At 0 V,  $C_{60}$  shows the smallest  $\Delta E_F = 1.03 \text{ eV}$ , CMC has an intermediate  $\Delta E_F = 1.07 \text{ eV}$ , while PCBM shows the highest

$\Delta E_F = 1.10 \text{ eV}$ . **Figure 6b** shows the voltage-dependent recombination currents of the three ETLs as a function of the applied bias. For voltages up to 0.9 V, the recombination current remains constant and then increases strongly with the voltage. In the case of a short circuit,  $C_{60}$  shows the smallest recombination current density ( $J_{rec}[0 \text{ V}] = 1.25 \text{ mA cm}^{-2}$ ), and for CMC  $J_{rec}(0 \text{ V}) = 1.72 \text{ mA cm}^{-2}$ ; however, PCBM shows a slightly larger recombination current density ( $J_{rec}[0 \text{ V}] = 2.55 \text{ mA cm}^{-2}$ ). Thus, the extraction of the photogenerated charges in  $C_{60}$  is the best while PCBM leads to the worst collection. This is in contrast to the lower series resistance measured for the cells with PCBM. The illuminated  $JV$

curves of the samples measured in Figures 4 and 6 are shown in Figure S21, Supporting Information. The CMC sample measured in Figure 4 has a lower  $FF_{RS} = 67\%$  compared to the cell measured for Figure 6,  $FF_{PL} = 77\%$ ; the cells with other ETLs behave similarly for both measurements. The series resistance, ideality factor, and equivalent of Figure 5f are shown in Figure S22, Supporting Information.

In addition to the voltage-dependent PL, the transient PL was measured on the HTL/perovskite/ETL device stack layers without BCP/Ag. Figure 6c shows the normalized PL decay as a function of time. Although the interpretation of tr-PL curves in multi-layer systems is sufficiently complicated because both transport and recombination are measured, we consider the tr-PL decay in the context of carrier extraction. Without a quencher, a rapid carrier loss is a sign of strong recombination, but when a transport layer is added, a rapid decrease in PL can also mean that the carriers are extracted efficiently.<sup>[27]</sup> Unlike the PL(V), no voltage can be applied to the layers; so, the half cells are always at open circuit. This means that transport and recombination processes always coexist and cannot easily be disentangled. Figure 6c shows a faster decay for  $C_{60}$  and a slower decay for PCBM and CMC, with PCBM decreasing faster at first but then slowing down while CMC decreases faster. As the observation is consistent with the good extraction for  $C_{60}$  from the PL(V) data, we assume that the tr-PL decay in this case is dominated by the transfer of electrons and holes to the ETL and HTL layers.

We then calculated the differential decay time

$$\tau_{\text{diff}} = -\frac{n(t)}{dn(t)/dt} = -\frac{2\phi(t)}{d\phi(t)/dt} \quad (3)$$

which assumes that the perovskite layer is well approximated as an intrinsic semiconductor; that is,  $\phi \propto np = n^2$  for the electron ( $n$ ) and hole ( $p$ ) densities encountered during the PL transient. Figure 6d shows the differential decay times from the curves fitted to the data in Figure 6c. The derivative is no longer plotted against time but against Fermi-level splitting, as described in ref. [61] A feature that stands out in Figure 6d is that the differential decay time continuously changes with  $\Delta E_F$  and does not provide a constant value that could be considered a recombination lifetime. To better understand the latter finding and further investigate the recombination processes, the next section discusses the tr-PL of the bare perovskite and perovskite with  $C_{60}$  on all four HTLs and Me-4PACz/Pero with different ETLs.

## 2.5. Non-Radiative Recombination Loss

For perovskite solar cells, non-radiative recombination at the perovskite–CTL interfaces plays a critical role in the recombination processes; and thus, for the  $V_{OC}$  of the device.<sup>[29]</sup> To characterize bulk and interface recombination losses, both steady-state and transient PL measurements are typically applied to a variety of layer stacks (from the film to the full device). From the differences between the different samples, conclusions are derived regarding the recombination activity of the bulk and the different interfaces. As this approach has been applied to both steady-state and transient PL,<sup>[61]</sup> the complexity of data interpretation differs significantly between the two methods. In steady-state PL applied to a series of samples with the same absorber but

different interfaces, the absolute PL intensity corrected for variations in outcoupling between the samples identifies differences in the rates of non-radiative recombination.<sup>[62,63]</sup> Lower PL intensities always identify situations in which the contribution of non-radiative recombination has increased. It is therefore deceptive to use steady-state PL quenching at the open circuit as a positive signal of charge extraction as it only probes the negative implications of having a junction between an absorber and contact layer.<sup>[64]</sup> In transient PL, the situation is somewhat different as currents can flow during the transient even in uncontacted films and layer stacks that do not allow current flow through an external circuit. Thus, dynamic effects such as the transfer of charge to contact layers can lead to faster decays as seen in Figure 6d, and superimpose the effects of non-radiative recombination. Thus, characterizing the recombination dynamics in multi-layer systems with interfaces and contact layers is challenging because of the superposition of transport, recombination, and capacitive effects that result from the charging or discharging of electrodes,<sup>[65]</sup> charge transport,<sup>[27]</sup> layers, or shallow defects.<sup>[66]</sup>

In the following, we compare both transient and steady-state PL and present a new approach to quantitatively disentangle the contributions of recombination to the transient PL from the contributions of transport and capacitive effects. For this purpose, we investigate three different layer stacks: ITO/HTL/Perovskite with the different HTLs, ITO/HTL/Perovskite/ $C_{60}$ , and ITO/Me-4PACz/Perovskite/ETL with the different ETLs. Figure 6c,d shows the tr-PL data and the derived decay time for one illumination intensity. To increase the range of the quasi-Fermi level splitting, we measure at three different laser intensities (2598, 258.2, and 25.4 nJ cm<sup>-2</sup>). Figure S25a–c, Supporting Information, shows the composite tr-PL decay for one example of each layer composition. Figure S25d–f, Supporting Information, then shows the derived differential decay times for all layer compositions. For layer stacks without ETL, a clear S-shape can be seen for all curves. We have previously identified pronounced S-shapes in simulations as originating from situations where substantial densities of charge carriers are re-injected into the pool of free carriers in the perovskite absorber at later times.<sup>[61]</sup> This re-injection can originate from HTL or ETL or be caused by detrapping from defects that have a high density but only interact efficiently with one band. Figure S27, Supporting Information, shows simulations with shallow defects that are filled during the early stages of the transient; and then, empty during later stages, thereby causing an S-shaped decay time curve. For the layers with ETL, the S-shape is less pronounced and the decay times at a given  $\Delta E_F$  are slightly shorter as compared to samples without ETL. At lower quasi-Fermi level splitting (later time), the differential decay time increases continuously until it runs into the limit determined by the lowest repetition rate ( $f_{\text{rep}} = 20$  kHz) of our system.

To disentangle recombination effects from transport and capacitive effects, one may express the differential equation for the electron density  $n$  in the perovskite absorber as:

$$\frac{dn}{dt} = -k_{\text{rad}}(np - n_i^2) - \beta_n n(N_t - n_t) + e_n n_t \quad (4)$$

the hole density  $p$  as

$$\frac{dp}{dt} = -k_{\text{rad}}(np - n_i^2) - \beta_p p n_t + e_p (N_t - n_t) \quad (5)$$

and the density of a trap state  $n_t$  as

$$\frac{dn_t}{dt} = \beta_n n (N_t - n_t) - \beta_p p n_t - e_n n_t + e_p (N_t - n_t) \quad (6)$$

Equations (4–6) assume an absorber layer with a single (relevant) trap state  $N_t$  that captures electrons and holes with the capture coefficients  $\beta_{n,p}$  and emits them back to the bands with the emission coefficients  $e_{n,p}$  that depend on the trap depth  $E_t$  via  $e_n = \beta_n N_c \exp(\frac{E_t - E_c}{kT})$  and  $e_p = \beta_p N_v \exp(\frac{E_v - E_t}{kT})$ .

If the density of trapped electrons hardly changes with time (i.e., if  $dn_t/dt \approx 0$ ),  $dn(t)/dt \approx -\bar{R}$  will be a good approximation. Here, the steady-state recombination rate  $\bar{R} = \bar{R}_{\text{rad}} + \bar{R}_{\text{SRH}}$ , whereby the terms on the right-hand side are the steady-state recombination rate for radiative and SRH recombination. This situation ( $dn(t)/dt \approx -\bar{R}$ ) is likely to be relevant, for instance, if we have a low density of deep defects without any significant rate of detrapping. Alternatively, if a defect becomes sufficiently shallow and its density becomes sufficiently high, trapping and detrapping rates become significant and  $dn/dt \neq -\bar{R}$ . Now, the rate  $dn_t/dt$  becomes significant; and hence, repopulating the conduction band with electrons by detrapping can become a relevant effect. Similarly, if we have a layer stack or a complete solar cell, the exchange of electrons and holes with other layers or electrodes can lead to  $dn/dt \neq -\bar{R}$  as now the reservoir of electrons and holes in the absorber may be repopulated by electrons from the ETL or holes from the HTL that had previously been transferred from the absorber to the transport layers.

All effects leading to  $dn/dt \neq -\bar{R}$  are capacitive in so far as they originate from charge carriers being temporarily stored in reservoirs (traps, other layers, electrodes) and then later being re-injected into the one charge-carrier reservoir that contributes to luminescence emission (the perovskite layer). Depending on the type of sample (film, layer stack, or full device), some of these effects may be absent. In a steady-state PL measurement at open circuit, we know that the average rates of recombination ( $\bar{R}$ ) and generation ( $G$ ) must be identical. Thus, we could determine an effective lifetime  $\tau_{\text{eff}}$  from the steady-state PL measured at a light intensity leading to an average generation  $G$  that would be given by  $\tau_{\text{eff}} = \bar{n}/\bar{G} = \bar{n}/\bar{R}$ . Furthermore, if recombination is dominant in the transient PL as well, the differential decay time obtained from Equation (3) is given by  $\tau_{\text{diff}} = \tau_{\text{eff}}$ . To identify the relative contributions of recombination versus capacitive effects to the decay time, we plot  $\tau_{\text{diff}}$  and  $\tau_{\text{eff}}$  into the same figure and compare their relative values as a function of either  $n$  or  $\Delta E_F$ . As these would be related by  $n = n_i \exp(\Delta E_F/2kT)$ , there would be no fundamental difference between the two options.

Analogously, as we can calculate the decay times for recombination from steady-state data, we can also perform the inverse operation if the assumption  $dn/dt = -\bar{R}$  was true. The steady-state PL data are often plotted as  $\Delta E_F$  versus generation rate or photon flux expressed in suns. This way of plotting the data allows one to directly see what the upper limit for  $V_{\text{OC}}$  would be that a layer (stack) without contacts would impose on any device that includes these layers and interfaces. If  $dn(t)/dt \approx -\bar{R}$  is a good approximation, we can assign an effective (steady-state) recombination or generation rate to the decay time via  $G = n/\tau_{\text{diff}}$  and determine the associated Fermi level splitting via  $\Delta E_F = 2kT \ln(n/n_i)$ .

In the following, we will illustrate these different mathematical operations for a perovskite layer on glass, a layer stack including the HTL, and one including both HTL and ETL. **Figure 7a** shows  $\tau_{\text{diff}}$  for three different laser intensities (solid lines) determined by Equation (3) as a function of  $\Delta E_F$ . Early times in the transient correspond to the data at high  $\Delta E_F$ , that is, it is intuitive to discuss this type of plot from the (lower) right to the (upper) left. Each branch of  $\tau_{\text{diff}}$  contains two distinguishable parts. At early times and a high  $\Delta E_F$ , the decay time increases rapidly until it approaches the dashed blue line. At this point, it changes its slope and increases more slowly than before toward lower values of  $\Delta E_F$ . Independent of the laser fluence and the initial carrier density, all decay times eventually approach the same slope at the second part of each decay time versus  $\Delta E_F$  curve. The symbols representing the decay time  $\tau_{\text{eff}}$  calculated from the steady-state data are slightly higher but still reasonably close to the blue dashed line. The dashed blue line has a constant slope that represents the ideality factor. For  $n = p$ , the slope would then follow from:

$$\tau_{\text{eff}} = \frac{\bar{n}}{\bar{R}(n)} \propto \exp\left(\frac{\Delta E_F}{kT} \left[\frac{1}{2} - \frac{1}{n_{\text{id}}}\right]\right) \quad (7)$$

Thus, a deep trap in high-level injection would cause  $n_{\text{id}} = 2$ ; and hence,  $\tau_{\text{eff}}$  would be constant as a function of  $\Delta E_F$ .<sup>[61,67]</sup> A recombination mechanism that causes  $n_{\text{id}}$  to become smaller than 2 (e.g., shallow trap or radiative recombination) would lead to an increase of  $\tau_{\text{eff}}$  toward lower values of  $\Delta E_F$ . We note that the ideality factor ( $n_{\text{id}} = 1.6$ ) that originates from the steady-state PL via

$$n_{\text{id}} = \frac{d\Delta E_F}{kT d \ln(G)} \quad (8)$$

is roughly identical to the ideality factor that is consistent with the slope of the tr-PL in **Figure 7a**. Thus, both the slope of  $\tau_{\text{diff}}$  versus  $\Delta E_F$  as well as the absolute value suggest that the decay times of the film on glass are primarily affected by recombination and not by trapping/detrapping effects at least in the part of the decay that is close to the blue dashed line in **Figure 7a**. At short times and high  $\Delta E_F$ ,  $\tau_{\text{diff}}$  increases rapidly with decreasing  $\Delta E_F$  which constitutes a clear deviation from the approximation  $dn(t)/dt \approx -R$ . In a perovskite film, this deviation can be explained either by charge-carrier diffusion or charge-carrier trapping. In the case of diffusion, the logic would be that the carrier density is not only a function of  $t$  but also a function of the spatial position  $x$  within the film. Therefore, the equation to be solved would be a partial differential equation of the form  $dn(t, x)/dt = -R(x, t) + D_n d^2n/dx^2$ , where  $D_n$  is the diffusion constant. The laser pulse creates more charge carriers close to the front surface than further away from it. As  $\phi \propto np = n^2$ , diffusion will lead to a homogenization of the carrier concentration; and in consequence, to a reduction in PL intensity even if the average density of charge carriers doesn't change.<sup>[68–71]</sup> In the case of carrier trapping, initially empty traps are filled by free electrons or holes, leading to a reduction in the PL that is faster than the rate of recombination.

**Figure 7b,c** shows the decay times calculated for perovskite films on Me-4PACz and Me-4PACz/perovskite/ $C_{60}$ , respectively. Interestingly, the decay times are higher than for the film on glass, and increase more steeply toward lower  $\Delta E_F$  which is

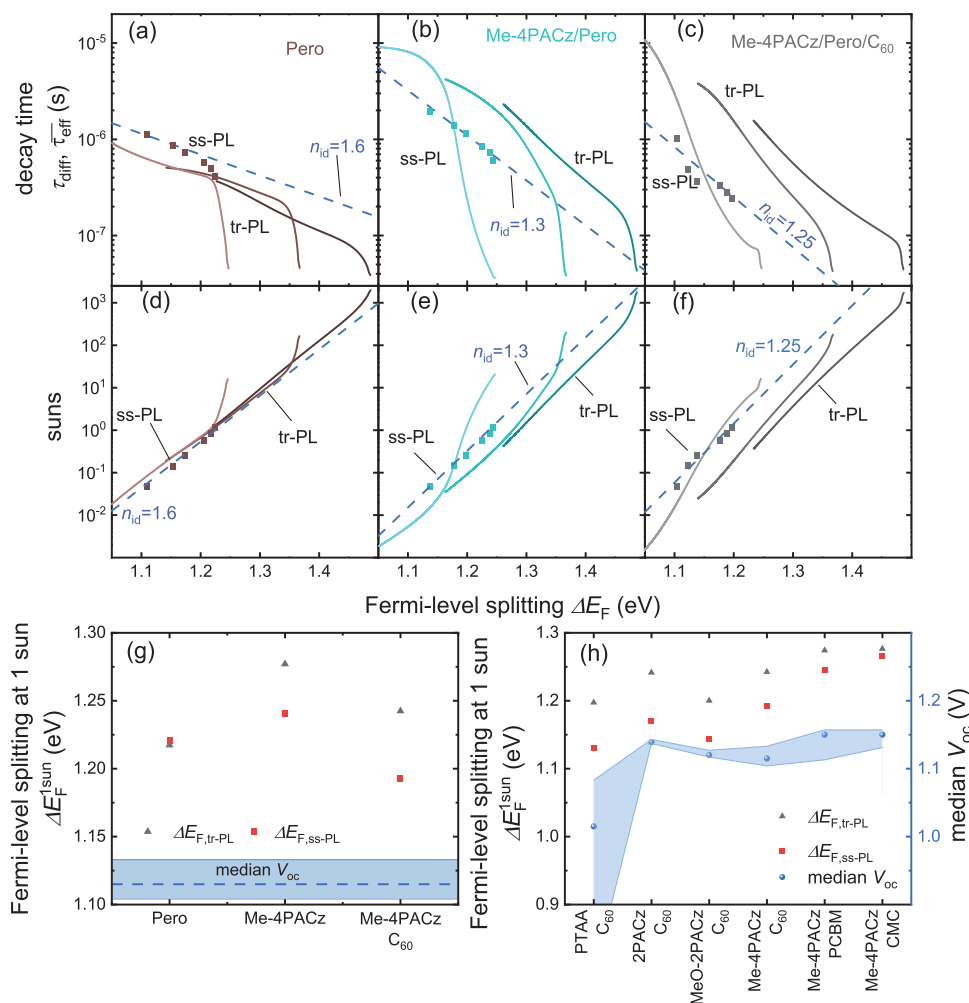


**Figure 7.** a–c) Decay times  $\tau_{diff}$  (solid lines) as derived from tr-PL measurements and  $\tau_{eff}$  from the steady-state PL are shown at different illumination intensities (squares). Dashed lines indicate the slope computed with Equation (7) that is consistent with the best-fitting ideality factor of the steady-state data. Perovskite on glass (a), perovskite on Me-4PACz (b), and half-cell with the stack Me-4PACz/Perovskite/ $C_{60}$  (c). d–f) Illumination intensity in Suns versus Fermi level splitting for ss-PL (squares) and tr-PL (lines). The dashed lines indicate the slopes corresponding to the ideality factors noted in the figure. For the same stacks as (a–c). g) Quasi-Fermi level splitting calculated from ss-PL (red squares) and tr-PL (black triangles) at one sun for perovskite on glass, on Me-4PACz, and on Me-4PACz covered with  $C_{60}$ . The median  $V_{oc}$  of the cell with the last configuration is shown as a dashed line, with the blue region representing 50% of the data, as shown by the box in Figure 3. h) Fermi-level splitting of different cell stacks from ss-PL (red squares), tr-PL (black triangles), and median  $V_{oc}$  (blue dots) of the respective cells.

consistent with a lower ideality factor (see blue dashed lines). In addition, we now observe significant differences between  $\tau_{diff}$  and  $\tau_{eff}$ . The decay time from tr-PL becomes longer while the decay time from the steady-state PL only slightly increases relative to the film on glass. Thus, we must be in a range, where the reservoir of free charge carriers in the perovskite is refilled to a significant extent at later times during the decay. Thus, either de-trapping or re-injection from the HTL must have a strong effect on the transient data but no effect on the steady-state data. In the presence of the  $C_{60}$  ETL, the shift between steady-state and transient PL decay times becomes even more pronounced. In Section S2.5.4, Supporting Information, we visualize the effect of de-trapping on the decay times from transient PL simulation, which shows that for a trap near the conduction band, the lifetime from ss-PL is indeed smaller than the tr-PL lifetime (Figure S32, Supporting Information).

Figure 7d–f mirrors the information content of Figure 7a–c by presenting each dataset from the above panel in the logic of steady-state PL. The squares represent the actual steady-state PL measurement while the lines represent the suns- $\Delta E_F$  data that are reconstructed from the transient PL under the assumption  $dn(t)/dt \approx -\bar{R}$ . The information content of Figure 6d–f is identical to Figure 6a–c and shows that the values of  $\Delta E_F$  that one would derive from transient PL are substantially higher than the values from the steady-state PL; and are, therefore not correct. They only serve to visualize the fact that the condition  $dn(t)/dt \approx -\bar{R}$  is not met in the samples with HTL or ETL.

Figure 7g shows the quasi-Fermi level splitting at one Sun for ss-PL and tr-PL, as well as the median  $V_{oc}$  of a cell with Me-4PACz and  $C_{60}$  as transport layers. As mentioned before, for perovskites on glass, there is no significant difference in  $\Delta E_F$  from ss-PL and tr-PL, the highest potential of  $\Delta E_F$ ; and thus, the



largest loss to the real cell has the layer on Me-4PACz without  $C_{60}$ . The  $C_{60}$  reduces the  $\Delta E_F$ , but when the traditional  $\Delta E_F$  from ss-PL is considered, the loss is not as big as in the tr-PL case. A comparison of the  $\Delta E_F$  from ss-PL and tr-PL with the respective median  $V_{OC}$  for the different HTL and ETL combinations is shown in Figure 7h; Figure S31, Supporting Information respectively. The difference between  $\Delta E_{F, ss-PL}$  and  $\Delta E_{F, tr-PL}$  is the largest for systems with  $C_{60}$ , decreases for PCBM, and decreases even more for CMC. The largest  $V_{OC}$  potential, that is, the largest  $\Delta E_F$ , is also found for CMC. However, the median  $V_{OC}$  of cells with CMC is not significantly larger than the median  $V_{OC}$  of cells with PCBM. Thus, the loss from half cell to cell is greatest for CMC. In addition, in the system with PTAA, a large loss between  $\Delta E_F$  and  $V_{OC}$  is observed.

### 3. Conclusion

The right choice of CTL is important for obtaining high efficiencies in perovskite solar cells because it affects both the recombination and efficient extraction of charge carriers. To minimize recombination and maximize the extraction efficiency, any CTL must fulfill a range of requirements, such as the right energy levels, good conductivity, and low interfacial recombination. In this study, we presented different methods for identifying and quantifying the properties that constitute a suitable HTL and ETL. Initially, we investigated the question of band alignment and found that the most severe obstacle for quantitative statements regarding the quality of band alignment is the uncertainty in the band edges of the perovskite relative to the vacuum. There are three different approaches to determine the valence band edge of the perovskite when measuring the energy level with UPS.<sup>[18–20]</sup> The combination with simulations showed that a value between the linear and logarithmic methods best reflects reality in the cells. Nevertheless, the exact band alignment between the transport layers and the perovskite cannot be determined. Therefore, other methods are required to quantify the offset between the perovskite and CTL. Here, we have examined electron-only devices with perovskite and fullerene and attempted to determine the barrier at the interface via the ratio of the reverse to the forward current. However, drift-diffusion simulations have shown that, unlike simple perovskite-only or fullerene-only devices, the formula for the built-in voltage<sup>[40]</sup> does not apply but the mobility of the fullerene significantly affects the ratio between  $J_r$  and  $J_f$ . In addition to band alignment, we studied charge transport in the cells by quantifying the series resistance for different HTLs and ETLs. The lowest series resistances were observed for the cells with MeO-2PACz/Pero/ $C_{60}$  and Me-4PACz/Pero/PCBM. A closer look at the losses in the  $FF$  shows that the CTL-to-CTL variations in  $FF$  losses are dominated by variations in  $R_s$  rather than variations in the ideality factor. Voltage-dependent and transient PL measurements show that charge extraction is most efficient in solar cells with  $C_{60}$  whereas samples with PCBM show significantly less efficient charge carrier extraction.

To better understand non-radiative recombination, steady-state PL and transient PL were investigated in combination. Layers without an ETL showed an S-shape, which could be reproduced in simulations by defects near the band edge. By comparing the Fermi-level splitting in a sum of tr-PL and ss-PL, it could be shown that for layer systems without ETL or with  $C_{60}$ ,

the Fermi-level splitting determined from the tr-PL was larger than that determined classically with ss-PL. In other words, the steady-state lifetime was shorter than the differential decay time from the tr-PL. This indicates an additional dynamic process that occurs at a later time, such as a detrapping effect from flat defects or re-injection of the charge carriers from  $C_{60}$  or one of the HTLs.

### Supporting Information

Supporting Information is available from the Wiley Online Library or from the author.

### Acknowledgements

J.S. and A.K. contributed equally to this work. The authors acknowledge support from the Helmholtz Association via the Helmholtz Young-Investigator Group Frontrunner and via the project-oriented funding (POF IV). The authors also acknowledge funding from the DFG for the project CREATIVE within the SPP “Perovskite Semiconductors: From Fundamental Properties to Devices” (SPP 2196) as well as GRK 2642. M.S. acknowledges funding by ProperPhotoMile. Project ProperPhotoMile is supported under the umbrella of SOLAR-ERA.NET Cofund 2 by the Spanish Ministry of Science and Education and the AEI under the project PCI2020-112185 and CDTI project number IDI-20210171; the Federal Ministry for Economic Affairs and Energy on the basis of a decision by the German Bundestag project numbers FKZ 03EE1070B and FKZ 03EE1070A and the Israel Ministry of Energy with project number 220-11-031. SOLAR-ERA.NET is supported by the European Commission within the EU Framework Programme for Research and Innovation HORIZON 2020 (Cofund ERA-NET Action, No. 786483), funded by the European Union. The views and opinions expressed; are, however, those of the author(s) only and do not necessarily reflect those of the European Union or the European Research Council Executive Agency (ERCEA). Neither the European Union nor the granting authority can be held responsible for them. The authors acknowledge funding from the European Research Council under the Horizon Europe program (LOCAL-HEAT, grant agreement no. 101041809).

Open access funding enabled and organized by Projekt DEAL.

### Conflict of Interest

The authors declare no conflict of interest.

### Data Availability Statement

The data that support the findings of this study are available from the corresponding author upon reasonable request.

### Keywords

built-in voltage, non-radiative recombination, perovskite, photoluminescence, series resistance, charge transport layers, solar cells

Received: February 11, 2023  
Revised: May 29, 2023  
Published online: July 10, 2023

- [1] J. Warby, F. Zu, S. Zeiske, E. Gutierrez-Partida, L. Frohloff, S. Kahmann, K. Frohna, E. Mosconi, E. Radicchi, F. Lang, S. Shah, F. Peña-Camargo, H. Hempel, T. Unold, N. Koch, A. Armin, F. De Angelis, S. D. Stranks, D. Neher, M. Stollerfoht, *Adv. Energy Mater.* **2022**, *12*, 2103567.

- [2] K. O. Brinkmann, T. Becker, F. Zimmermann, C. Kreusel, T. Gahlmann, M. Theisen, T. Haeger, S. Olthof, C. Tückmantel, M. Günster, T. Maschwitz, F. Göbelsmann, C. Koch, D. Hertel, P. Caprioglio, F. Peña-Camargo, L. Perdigón-Toro, A. Al-Ashouri, L. Merten, A. Hinderhofer, L. Gomell, S. Zhang, F. Schreiber, S. Albrecht, K. Meerholz, D. Neher, M. Stollerfoht, T. Riedl, *Nature* **2022**, 604, 280.
- [3] M. Stollerfoht, C. M. Wolff, J. A. Márquez, S. Zhang, C. J. Hages, D. Rothhardt, S. Albrecht, P. L. Burn, P. Meredith, T. Unold, D. Neher, *Nat. Energy* **2018**, 3, 847.
- [4] S. Cacovich, G. Vidon, M. Degani, M. Legrand, L. Gouda, J.-B. Puel, Y. Vaynzof, J.-F. Guillemoles, D. Ory, G. Grancini, *Nat. Commun.* **2022**, 13, 2868.
- [5] H. Chen, S. Teale, B. Chen, Y. Hou, L. Grater, T. Zhu, K. Bertens, S. M. Park, H. R. Atapattu, Y. Gao, M. Wei, A. K. Johnston, Q. Zhou, K. Xu, D. Yu, C. Han, T. Cui, E. H. Jung, C. Zhou, W. Zhou, A. H. Proppe, S. Hoogland, F. Laquai, T. Filleter, K. R. Graham, Z. Ning, E. H. Sargent, *Nat. Photonics* **2022**, 16, 352.
- [6] Q. Jiang, J. Tong, Y. Xian, R. A. Kerner, S. P. Dunfield, C. Xiao, R. A. Scheidt, D. Kuciauskas, X. Wang, M. P. Hautzinger, R. Tirawat, M. C. Beard, D. P. Fenning, J. J. Berry, B. W. Larson, Y. Yan, K. Zhu, *Nature* **2022**, 611, 278.
- [7] A. Magomedov, A. Al-Ashouri, E. Kasparavičius, S. Strazdaite, G. Niaura, M. Jošt, T. Malinauskas, S. Albrecht, V. Getautis, *Adv. Energy Mater.* **2018**, 8, 1801892.
- [8] A. Al-Ashouri, A. Magomedov, M. Roß, M. Jošt, M. Talaikis, G. Chistiakova, T. Bertram, J. A. Márquez, E. Köhnen, E. Kasparavičius, S. Levenco, L. Gil-Escrig, C. J. Hages, R. Schlatmann, B. Rech, T. Malinauskas, T. Unold, C. A. Kaufmann, L. Korte, G. Niaura, V. Getautis, S. Albrecht, *Energy Environ. Sci.* **2019**, 12, 3356.
- [9] Z. Liu, J. Siekmann, B. Klingebiel, U. Rau, T. Kirchartz, *Adv. Energy Mater.* **2021**, 11, 2003386.
- [10] V. M. Le Corre, M. Stollerfoht, L. Perdigón Toro, M. Feuerstein, C. Wolff, L. Gil-Escrig, H. J. Bolink, D. Neher, L. J. A. Koster, *ACS Appl. Energy Mater.* **2019**, 2, 6280.
- [11] O. J. Sandberg, J. Kurpiers, M. Stollerfoht, D. Neher, P. Meredith, S. Shoaee, A. Armin, *Adv. Mater. Interfaces* **2020**, 7, 2000041.
- [12] D. Grabowski, Z. Liu, G. Schöpe, U. Rau, T. Kirchartz, *Sol. RRL* **2022**, 6, 2200507.
- [13] S. Tan, T. Huang, I. Yavuz, R. Wang, T. W. Yoon, M. Xu, Q. Xing, K. Park, D.-K. Lee, C.-H. Chen, R. Zheng, T. Yoon, Y. Zhao, H.-C. Wang, D. Meng, J. Xue, Y. J. Song, X. Pan, N.-G. Park, J.-W. Lee, Y. Yang, *Nature* **2022**, 605, 268.
- [14] R. Wang, J. Xue, K.-L. Wang, Z.-K. Wang, Y. Luo, D. Fenning, G. Xu, S. Nuryeva, T. Huang, Y. Zhao, J. L. Yang, J. Zhu, M. Wang, S. Tan, I. Yavuz, K. N. Houk, Y. Yang, *Science* **2019**, 366, 1509.
- [15] J. Peng, F. Kremer, D. Walter, Y. Wu, Y. Ji, J. Xiang, W. Liu, T. Duong, H. Shen, T. Lu, F. Brink, D. Zhong, L. Li, O. Lee Cheong Lem, Y. Liu, K. J. Weber, T. P. White, K. R. Catchpole, *Nature* **2022**, 601, 573.
- [16] A. Al-Ashouri, E. Köhnen, B. Li, A. Magomedov, H. Hempel, P. Caprioglio, J. A. Márquez, A. B. M. Vilches, E. Kasparavičius, J. A. Smith, N. Phung, D. Menzel, M. Grischek, L. Kegelmann, D. Skroblin, C. Gollwitzer, T. Malinauskas, M. Jošt, G. Matič, B. Rech, R. Schlatmann, M. Topič, L. Korte, A. Abate, B. Stannowski, D. Neher, M. Stollerfoht, T. Unold, V. Getautis, S. Albrecht, *Science* **2020**, 370, 1300.
- [17] T. Hellmann, C. Das, T. Abzieher, J. A. Schwenzer, M. Wussler, R. Dachauer, U. W. Paetzold, W. Jaegermann, T. Mayer, *Adv. Energy Mater.* **2020**, 10, 2002129.
- [18] J. Endres, D. A. Egger, M. Kulbak, R. A. Kerner, L. Zhao, S. H. Silver, G. Hodes, B. P. Rand, D. Cahen, L. Kronik, A. Kahn, *J. Phys. Chem. Lett.* **2016**, 7, 2722.
- [19] P. Schulz, D. Cahen, A. Kahn, *Chem. Rev.* **2019**, 119, 3349.
- [20] F. Zhang, S. H. Silver, N. K. Noel, F. Ullrich, B. P. Rand, A. Kahn, *Adv. Energy Mater.* **2020**, 10, 1903252.
- [21] T. C. M. Müller, B. E. Pieters, U. Rau, T. Kirchartz, *J. Appl. Phys.* **2013**, 113, 134503.
- [22] M. Wolf, H. Rauschenbach, *Adv. Energy Convers.* **1963**, 3, 455.
- [23] M. Stollerfoht, V. M. Le Corre, M. Feuerstein, P. Caprioglio, L. J. A. Koster, D. Neher, *ACS Energy Lett.* **2019**, 4, 2887.
- [24] U. Rau, V. Huhn, B. E. Pieters, *Phys. Rev. Appl.* **2020**, 14, 014046.
- [25] L. Wagner, P. Schygulla, J. P. Herterich, M. Elshamy, D. Bogachuk, S. Zouhair, S. Mastroianni, U. Würfel, Y. Liu, S. M. Zakeeruddin, M. Grätzel, A. Hinsch, S. W. Glunz, *Matter* **2022**, 5, 2352.
- [26] T. Du, W. Xu, S. Xu, S. R. Ratnasingham, C.-T. Lin, J. Kim, J. Briscoe, M. A. McLachlan, J. R. Durrant, *J. Mater. Chem. C* **2020**, 8, 12648.
- [27] B. Krogmeier, F. Staub, D. Grabowski, U. Rau, T. Kirchartz, *Sustainable Energy Fuels* **2018**, 2, 1027.
- [28] A. Kulkarni, R. Sarkar, S. Akel, M. Haeser, B. Klingebiel, M. Wuttig, S. Chakraborty, M. Saliba, T. Kirchartz, arXiv preprint arXiv:2302.05547 **2023**.
- [29] J. Haddad, B. Krogmeier, B. Klingebiel, L. Krückemeier, S. Melhem, Z. Liu, J. Hüpkens, S. Mathur, T. Kirchartz, *Adv. Mater. Interfaces* **2020**, 7, 2000366.
- [30] P. Caprioglio, C. M. Wolff, O. J. Sandberg, A. Armin, B. Rech, S. Albrecht, D. Neher, M. Stollerfoht, *Adv. Energy Mater.* **2020**, 10, 2000502.
- [31] J. Diekmann, P. Caprioglio, M. H. Futscher, V. M. Le Corre, S. Reichert, F. Jaiser, M. Arvind, L. P. Toro, E. Gutierrez-Partida, F. Peña-Camargo, C. Deibel, B. Ehrler, T. Unold, T. Kirchartz, D. Neher, M. Stollerfoht, *Sol. RRL* **2021**, 5, 2100219.
- [32] G. Ertl, J. Küppers, *Low energy electrons and surface chemistry*, VCH Weinheim **1985**.
- [33] E. A. Kraut, R. W. Grant, J. R. Waldrop, S. P. Kowalczyk, *Phys. Rev. Lett.* **1980**, 44, 1620.
- [34] D. Menzel, A. Tejada, A. Al-Ashouri, I. Levine, J. A. Guerra, B. Rech, S. Albrecht, L. Korte, *ACS Appl. Mater. Interfaces* **2021**, 13, 43540.
- [35] M. Burgelman, P. Nollet, S. Degraeve, *Thin Solid Films* **2000**, 361–362, 527.
- [36] N. F. Mott, R. W. Gurney, *Electronic Processes in Ionic Crystals*, Clarendon Press, **1948**.
- [37] L. M. Herz, *ACS Energy Lett.* **2017**, 2, 1539.
- [38] M. A. Lampert, P. Mark, *Current Injection in Solids*, Academic Press, Cambridge, MA **1970**.
- [39] J. Siekmann, S. Ravishankar, T. Kirchartz, *ACS Energy Lett.* **2021**, 6, 3244.
- [40] J. A. Röhr, *Phys. Rev. Appl.* **2019**, 11, 054079.
- [41] J. A. Röhr, D. Moia, S. A. Haque, T. Kirchartz, J. Nelson, *J. Phys.: Condens. Matter* **2018**, 30, 105901.
- [42] M. A. Lampert, *Rep. Prog. Phys.* **1964**, 27, 329.
- [43] E. A. Duijnste, J. M. Ball, V. M. Le Corre, L. J. A. Koster, H. J. Snaith, J. Lim, *ACS Energy Lett.* **2020**, 5, 376.
- [44] V. M. Le Corre, E. A. Duijnste, O. El Tambouli, J. M. Ball, H. J. Snaith, J. Lim, L. J. A. Koster, *ACS Energy Lett.* **2021**, 6, 1087.
- [45] M. Sajedi Alvar, P. W. M. Blom, G.-J. A. H. Wetzelaer, *Nat. Commun.* **2020**, 11, 4023.
- [46] J. A. Röhr, T. Kirchartz, J. Nelson, *J. Phys.: Condens. Matter* **2017**, 29, 205901.
- [47] R. E. Schropp, M. Zeman, *Amorphous and Microcrystalline Silicon Solar Cells: Modeling, Materials and Device Technology*, Springer, Berlin **1998**.
- [48] B. E. Pieters, J. Krc, M. Zeman, in 2006 IEEE 4th World Conference on Photovoltaic Energy Conference, Vol. 2, IEEE, Piscataway, NJ **2006**, p. 1513.
- [49] W. Rehman, D. P. McMeekin, J. B. Patel, R. L. Milot, M. B. Johnston, H. J. Snaith, L. M. Herz, *Energy Environ. Sci.* **2017**, 10, 361.

- [50] D. P. McMeekin, Z. Wang, W. Rehman, F. Pulvirenti, J. B. Patel, N. K. Noel, M. B. Johnston, S. R. Marder, L. M. Herz, H. J. Snaith, *Adv. Mater.* **2017**, 29, 1607039.
- [51] D. P. McMeekin, G. Sadoughi, W. Rehman, G. E. Eperon, M. Saliba, M. T. Hörantner, A. Haghighirad, N. Sakai, L. Korte, B. Rech, M. B. Johnston, L. M. Herz, H. J. Snaith, *Science* **2016**, 351, 151.
- [52] P.-W. Liang, C.-C. Chueh, S. T. Williams, A. K.-Y. Jen, *Adv. Energy Mater.* **2015**, 5, 1402321.
- [53] P. H. Nguyen, S. Scheinert, S. Berleb, W. Brütting, G. Paasch, *Org. Electron.* **2001**, 2, 105.
- [54] M. Cheng, C. Zuo, Y. Wu, Z. Li, B. Xu, Y. Hua, L. Ding, *Sci. Bull.* **2020**, 65, 1237.
- [55] A. G. Aberle, S. R. Wenham, M. A. Green, Conference Record of the Twenty Third IEEE Photovoltaic Specialists Conference –1993 (Cat. No.93CH3283-9) **1993**, 133.
- [56] D. Pysch, A. Mette, S. W. Glunz, *Sol. Energy Mater. Sol. Cells* **2007**, 91, 1698.
- [57] T. Kirchartz, J. Nelson, *Phys. Rev. B* **2012**, 86, 165201.
- [58] U. Rau, B. Blank, T. C. M. Müller, T. Kirchartz, *Phys. Rev. Appl.* **2017**, 7, 044016.
- [59] L. Krückemeier, U. Rau, M. Stollerfoht, T. Kirchartz, *Adv. Energy Mater.* **2020**, 10, 1902573.
- [60] A. Dasgupta, S. Mahesh, P. Caprioglio, Y.-H. Lin, K.-A. Zaininger, R. D. J. Oliver, P. Holzhey, S. Zhou, M. M. McCarthy, J. A. Smith, M. Frenzel, M. G. Christoforo, J. M. Ball, B. Wenger, H. J. Snaith, *ACS Energy Lett.* **2022**, 7, 2311.
- [61] L. Krückemeier, B. Krogmeier, Z. Liu, U. Rau, T. Kirchartz, *Adv. Energy Mater.* **2021**, 11, 2003489.
- [62] M. Stollerfoht, P. Caprioglio, C. M. Wolff, J. A. Márquez, J. Nordmann, S. Zhang, D. Rothhardt, U. Hörmann, Y. Amir, A. Redinger, L. Kegelmann, F. Zu, S. Albrecht, N. Koch, T. Kirchartz, M. Saliba, T. Unold, D. Neher, *Energy Environ. Sci.* **2019**, 12, 2778.
- [63] M. Stollerfoht, M. Grischek, P. Caprioglio, C. M. Wolff, E. Gutierrez-Partida, F. Peña-Camargo, D. Rothhardt, S. Zhang, M. Raoufi, J. Wolansky, M. Abdi-Jalebi, S. D. Stranks, S. Albrecht, T. Kirchartz, D. Neher, *Adv. Mater.* **2020**, 32, 2000080.
- [64] E. M. Hutter, T. Kirchartz, B. Ehrler, D. Cahen, E. v. Hauff, *Appl. Phys. Lett.* **2020**, 116, 100501.
- [65] D. Kiermasch, A. Baumann, M. Fischer, V. Dyakonov, K. Tvingstedt, *Energy Environ. Sci.* **2018**, 11, 629.
- [66] C. J. Hages, A. Redinger, S. Levchenko, H. Hempel, M. J. Koeper, R. Agrawal, D. Greiner, C. A. Kaufmann, T. Unold, *Adv. Energy Mater.* **2017**, 7, 1700167.
- [67] L. Krückemeier, Z. Liu, B. Krogmeier, U. Rau, T. Kirchartz, *Adv. Energy Mater.* **2021**, 11, 2102290.
- [68] G. S. Kousik, Z. G. Ling, P. K. Ajmera, *J. Appl. Phys.* **1992**, 72, 141.
- [69] T. Otaredian, *Solid-State Electron.* **1993**, 36, 153.
- [70] F. Staub, I. Anusca, D. C. Lupascu, U. Rau, T. Kirchartz, *JPhys Mater.* **2020**, 3, 025003.
- [71] C. Cho, S. Feldmann, K. M. Yeom, Y.-W. Jang, S. Kahmann, J.-Y. Huang, T. C. J. Yang, M. N. T. Khayyat, Y.-R. Wu, M. Choi, J. H. Noh, S. D. Stranks, N. C. Greenham, *Nat. Mater.* **2022**, 21, 1388.